


Hypersonic Surface Phononic Bandgap Demonstration in a CMOS-Compatible Pillar-Based Piezoelectric Structure on Silicon

Razi Dehghannasiri, Ali Asghar Eftekhari, and Ali Adibi*

School of Electrical and Computer Engineering, Georgia Institute of Technology, Atlanta, Georgia 30332, USA

 (Received 30 August 2017; revised manuscript received 7 February 2018; published 7 December 2018)

We demonstrate a new phononic crystal (PnC) platform with wideband hypersonic phononic bandgaps (PnBGs) for surface acoustic waves (SAWs). These SAW PnCs are fabricated on a CMOS-compatible substrate and constructed by a two-dimensional periodic array of piezoelectric aluminium nitride pillars on silicon to achieve a low-loss all-dielectric PnC platform. Our experimental PnBG results acquired with integrated wideband SAW filters (i.e., two slanted interdigital transducers as an emitter and a receiver) show a surface PnBG from 1.6 to 1.75 GHz for the fabricated surface PnC, enabling the formation of low-loss hypersonic PnC-based devices for a wide range of ultrahigh-frequency applications, including wireless communications.

DOI: [10.1103/PhysRevApplied.10.064019](https://doi.org/10.1103/PhysRevApplied.10.064019)

I. INTRODUCTION

Surface acoustic waves (SAWs)—a class of acoustic waves confined within a few wavelengths from the surface of a semi-infinite elastic medium—range from giant seismic waves with kilometer wavelengths on the surface of Earth [1] to tiny traveling ripples on the surface of a chip with micron wavelengths [2]. Microfabricated SAW-based devices are integral parts of many filtering and duplexing applications in wireless communications [2,3] because of the ease of surface micromachining in mass production and scalability of the operation frequency by adjustment of the lateral dimensions. As the working frequency of SAW devices is set by surface-feature sizes, wireless devices supporting a multitude of spectral bands (e.g., Long-Term Evolution, Global Positioning System, and Wi-Fi) can be fabricated by co-integration of SAW devices on a single chip. SAW devices have been also investigated in quantum studies [4–9] and in conjunction with photonic crystal cavities for dynamic modulation of optical signals [10–12].

The ability to control the propagation of SAWs in periodic structures has motivated researchers to extensively investigate SAW phononic crystals (PnCs) [13–25], artificially created surface periodic structures supporting a phononic bandgap (PnBG) [26–29] for SAWs. A complete PnBG is a range of frequencies in which the propagation of acoustic waves in any direction within the defect-free PnC is prohibited. Therefore, similarly to the case of its optical counterpart (i.e., a *photonic crystal* [30]), introduction of an appropriate defect [31,32] inside a perfect SAW

PnC allows low-loss localization and navigation of surface acoustic phonons within PnBG frequencies.

SAW PnCs are created by periodically varying the effective elastic properties (i.e., mass density and stiffness) on the surface of host materials in one or two dimensions (e.g., through ordered synthesis and/or perforation). SAW PnCs are broadly classified as hole-based SAW PnCs [14,17–19] and pillar-based SAW PnCs [21,24,25]. In comparison with hole-based SAW PnCs, pillar-based SAW PnCs are more promising in terms of wider PnBGs in the ultrasound (megahertz) and hypersound (gigahertz) regimes, with less stringent fabrication constraints because of the additional design flexibility in selecting the geometry and material of the pillars. PnBGs in pillar-based PnCs [21] stem from the interplay of both Bragg scattering from the periodic phononic structure and local resonances of the individual pillar (i.e., lattice sites). Depending on the frequency of the propagating SAWs in the lattice, pillars can act as either local scatterers or local resonators, which is determined by the geometry and elastic properties of the individual pillar and the global symmetry of the lattice [23]. Likewise, in pillar-based membrane PnCs [33–36], where the thickness of the substrate is comparable to or smaller than the wavelength of the acoustic wave, PnBGs appear as a result of the resonances of the pillars, with noticeable flat phononic dispersion bands.

Previous experimental work on pillar-based SAW PnCs was mostly based on deposited metallic pillars [21,24]. These platforms have enabled the formation of wideband SAW PnBGs below the substrate sound line. However, this wideband PnBG is achieved at the price of extra phononic loss of metals for acoustic waves [37,38]. Therefore, the realization of SAW-PnC devices with wide PnBG and low

*ali.adibi@ece.gatech.edu

phononic losses based on nonmetallic structures is of great importance.

This study is, to the best of our knowledge, the first report on experimental demonstration of a SAW PnC based on nonmetallic pillars at hypersonic frequencies on a CMOS-compatible piezoelectric platform. Such structures allow direct integration of SAW-based devices with radio-frequency (rf) electronics. In Sec. II, we discuss dissipation processes in phononic devices and compare metallic pillars and dielectric pillars in terms of major intrinsic losses. In Sec. III, we discuss our simulation results and describe our design approach for both the SAW PnC and the wideband interdigital transducers (IDTs) used for PnBG characterization. In Sec. IV, we discuss the fabrication process and the experimental characterization results of the fabricated SAW-PnC devices. Final conclusions are given in Sec. V.

II. PHONONIC MATERIAL LOSS IN PnC STRUCTURES: METALLIC PILLARS VERSUS NONMETALLIC PILLARS

The design of a low-loss phononic structure requires mitigation of acoustic loss through different extrinsic and intrinsic processes, such as coupling to radiative acoustic modes, thermoelastic damping, phonon-phonon interaction, and phonon-electron scattering [39,40]. With the suppression of radiation loss (or coupling to bulk modes) in surface PnC structures through appropriate design of PnC defects [31], thermoelastic damping becomes the primary loss mechanism in PnC structures [41–46]. The thermoelastic damping is caused by the irreversible conversion (or coupling) of the strain energy to heat due to thermal diffusion. Thermoelastic loss is, in general, greater in metals [38,42,47] due to the larger thermal diffusivity (i.e., $D = \kappa/C_p$, where κ and C_p are the thermal conductivity and specific heat capacity at constant pressure, respectively) and larger linear thermal expansion coefficients [i.e., $\alpha = \partial(\ln L)/\partial T$]. Landau and Lifshitz [44] showed the thermoelastic damping generally scales as $\gamma \sim \kappa\alpha^2/C_p^2$. Table I compares γ as an indication of thermoelastic loss in selected dielectric and metallic materials. As is clear from Table I, metallic materials have much higher thermoelastic damping losses than dielectric materials. In addition, dielectric structures are much less prone to electron-phonon-scattering losses [40] than metals. Electron-phonon scattering is one of the major sources of acoustic dissipation for ultrasonic acoustic waves in bulk metals at low temperatures [40,49]. In addition to the intrinsic losses (i.e., thermoelastic and phonon-electron dissipations) in metals, the friction at metal-piezoelectric

interfaces in PnC structures formed by metallic pillars on a piezoelectric substrate also contributes to the overall phononic loss [50,51]. Similarly to the case of metallic-pillar PnC structures, the use of metallic electrodes in directly excited PnC structures will lead to increased acoustic losses. Recently, it was demonstrated that by use of capacitive excitation and avoidance of direct-contact metallic electrodes in a piezoelectric membrane structure, the mechanical quality factor (Q_{ph}) of the membrane structure at 1.2 GHz can be significantly increased [51]. These observations show that the use of nonmetallic pillars results in surface PnC devices with potentially higher Q_{ph} than those based on metallic-based PnC platforms.

III. SURFACE PnC BAND STRUCTURE AND WIDEBAND IDT DESIGN

Silicon (Si) is a crystalline substrate suitable for fabricating phononic devices due to the availability of mature fabrication techniques, ease of integration with CMOS electronic circuitry, and low acoustic losses. However, Si is not a piezoelectric material. Thus, a piezoelectric film on Si is required to enable efficient excitation and detection of SAWs through IDTs [2,52]. Thin-film aluminum nitride (AlN) [53] is a CMOS-compatible material that can fulfill the role of an electromechanical transducer while enabling the formation of a surface PnC by patterning it into pillar structures. AlN has recently received attention in piezo-optomechanical studies (e.g., Refs. [12,54,55]), but discussion of this is beyond the scope of this paper.

A. Elastic wave simulations in surface PnC structures

Radiation loss of SAW-PnC devices (primarily caused by coupling of surface-confined waves of the devices to bulk waves) and the existence of the PnBG depend on the extent of the nonradiative spectral region, which is set by the slowest bulk mode of the substrates and the PnC lattice symmetries. Among the various two-dimensional lattice structures, the triangular lattice provides the largest nonradiative wavevector extent for a certain lattice constant [23]. Figure 1 provides the simulated surface phononic band structure of the conelike AlN pillars in a triangular lattice on (100)-oriented Si with a primary surface PnBG from 1.6 to 1.74 GHz. As shown in Fig. 1(a), the edges of the irreducible Brillouin zone (IBZ) of the PnC structure are Γ - X - L - K - Γ due to the elastic anisotropy in Si and symmetry of the PnC lattice.

The phononic band structure in Fig. 1 is calculated for a primitive unit cell of the SAW PnC by the finite-element

TABLE I. Thermoelastic damping of various metals and dielectrics [38,48].

	Si	AlN	W	Au	Ni	Al	Cu	Pt	SiC
$\gamma \sim \kappa\alpha^2/C_p^2$	0.0017	0.0026	0.32	3.8	0.08	0.15	0.88	0.32	0.0007

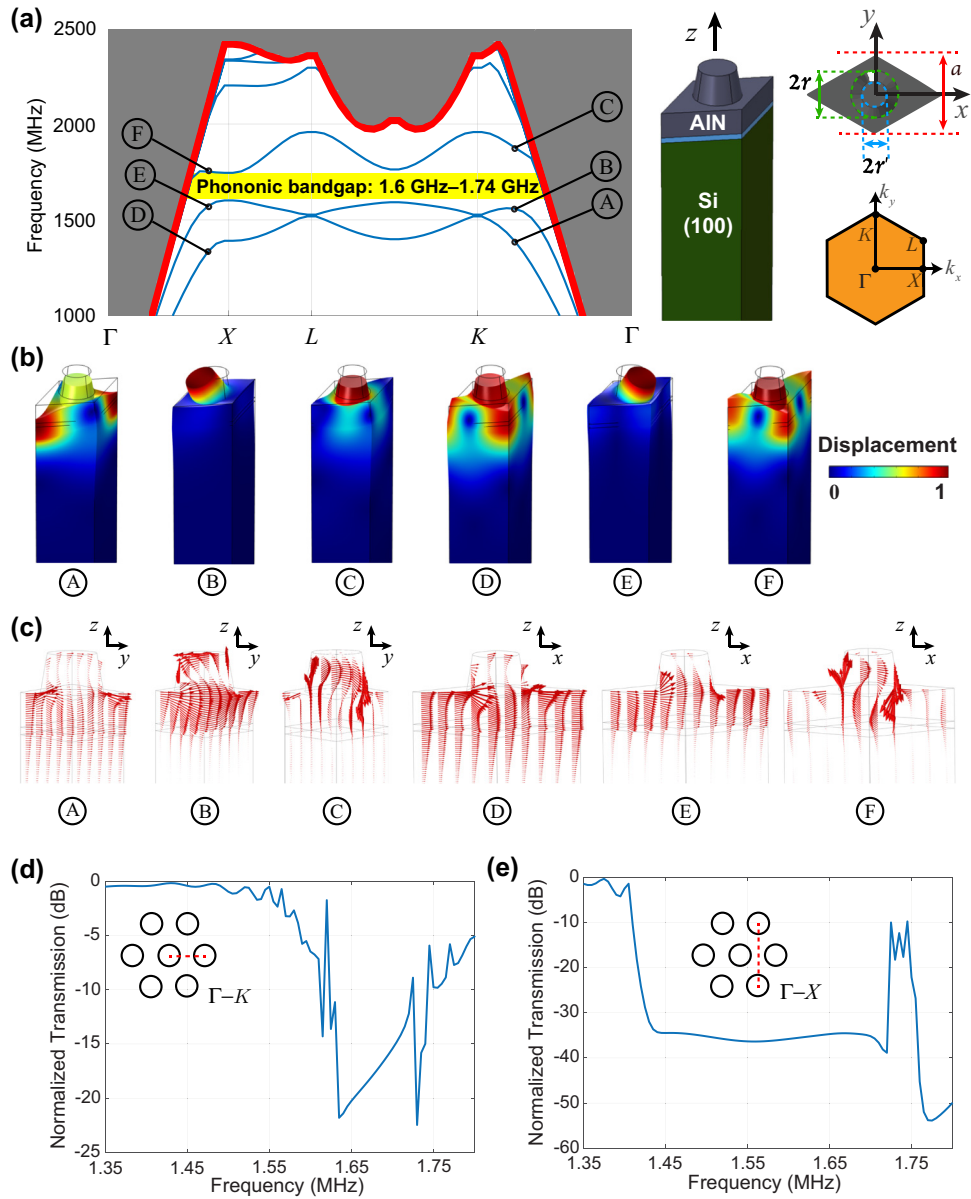


FIG. 1. (a) Simulated surface phononic band structure of the fabricated SAW PnC, which is a triangular lattice of conelike AlN pillars on a (100)-oriented Si substrate (see the schematic of the lattice primitive unit cell) over the edges of the IBZ. The region shaded yellow specifies the extent of the theoretical complete surface PnBG from 1.6 to 1.74 GHz. The lattice constant a (i.e., the distance between the nearest adjacent pillars) of the simulated PnC is $1.4 \mu\text{m}$, and the angle, height, and top radius of the cone (i.e., r') are 80° , 530 nm , and 340 nm , respectively. (b) Displacement profiles of selected points from the dispersion bands of the PnC structure in (a). (c) The acoustic power flow of the SAW-PnC unit cell corresponding to the mode profiles shown in (b). Small red arrows show the density and direction of the power flow in the midplane of the unit cell (i.e., in the plane of $x = 0$ for modes A, B, and C, and in the plane of $y = 0$ for modes D, E, and F). For the modes propagating in the Γ - K and Γ - X directions, the flow of the acoustic power is along the y and x directions, respectively, as seen from (c). (d),(e) Simulated phononic transmission along Γ - K (11 layers: $11 \times a$) and Γ - X (nine layers: $9 \times a/\sqrt{3}$), respectively.

method in the COMSOL MULTIPHYSICS environment [56]. The material constants used in this simulation are listed in Table II. Figure 1(a) shows the coordinate axes of the simulation domain, in which the c axis of AlN and the Z axis of the Si stiffness tensor are along the z axis of the simulation domain, and the X and Y axes of the Si stiffness

tensor are along the x and y axes of the simulation domain, respectively. By applying the Floquet periodic boundary condition to the boundaries of the primitive unit cell perpendicular to the x - y plane and setting the wavenumber ($k_x, k_y \in \text{IBZ}$, $k_z = 0$), we find the corresponding eigenfrequency and eigenmodes, and extract the band structure

TABLE II. Material constants of AlN and Si used in the simulations.

	Symbol	AlN	Si
Elastic constants (GPa)	c_{11}	345	165.6
	c_{12}	125	63.9
	c_{13}	120	63.9
	c_{33}	395	165.6
	c_{44}	118	79.5
	c_{66}	110	79.5
Piezoelectric constants (C/m ²)	e_{x5}	-0.48	-
	e_{z1}	-0.58	-
	e_{z3}	1.55	-
Mass density (kg/m ³)	ρ	3260	2330
Relative permittivities	ϵ_{xx}/ϵ_0	8	11.7
	ϵ_{zz}/ϵ_0	9.5	11.7

of the surface acoustic modes propagating through the lattice in the x - y plane. In Fig. 1(a), the thin blue curves denote the confined surface phononic modes of the PnC structure, and the thick red line (i.e., the slowest shear bulk mode) represents the border between the phononic modes well bounded to the surface and the radiative modes (i.e., the bulk modes or leaky surface modes—gray region) not confined to the surface.

Our simulation results reveal that to achieve a wide PnBG, it is critical to have close-to-vertical sidewalls. In addition, simulations show that for thin AlN pedestals, the PnC lattice constant (i.e., a) does not play a major role in adjusting the width and center frequency of the first (primary) PnBG. However, as the thickness of the AlN pedestal increases, both the width of the first PnBG and its dependence on the PnC lattice constant increase, indicating that both Bragg scattering and local resonances contribute to the PnBG. Also, at the vicinity of the maximum radius for the pillars, we observe a weak relation between the PnBG and the radius of the pillars. To find the optimum structure in terms of the bandgap width, we fix the angle of the pillars to be 80° as determined by our fabrication process, the filling fraction [i.e., $(2\pi/\sqrt{3})(r/a)^2$] to be between 0.3 and 0.45 (for ease of fabrication), and the total height of the AlN layer (i.e., height of the pillars plus the thickness of the pedestal) to be $1 \mu\text{m}$. Therefore, the optimization parameters reduce in number to three; namely, the height of the pillars, which accordingly sets the thickness of the pedestal, the lattice constant, and the filling fraction (or the pillar radius, r). By finely sweeping these parameters, we find that by selecting $a = 1.40 \mu\text{m}$, $r = 430 \text{ nm}$, and a pillar height of 530 nm , we can obtain a wide 0.14-GHz SAW PnBG centered at 1.67 GHz [see Fig. 1(a) for the definition of the parameters]. In this optimization process, the high frequency of the PnBG is the first priority, and the width of the PnBG is the secondary criterion. While we keep some parameters fixed (e.g., AlN

thickness and pillar angles) to reduce the fabrication complexity, changing these parameters might result in better characteristics (e.g., wider PnBG) at the cost of fabrication complexity. Nevertheless, the simulated PnBG width obtained in our optimization is enough for all practical applications.

To get more insight into the types of surface phononic modes in the PnC structure, we illustrate in Fig. 1(b) the displacement profile of selected points from the phononic band structure shown in Fig. 1(a) for $ak_y = 3.5$ along Γ - K and $ak_x = 3.2$ along Γ - X . Figure 1(c) illustrates the density and direction of the acoustic power flow in the PnC unit cell. For the modes in the Γ - K and Γ - X directions, the flow of the acoustic power is along the y and x directions, respectively, as seen from Fig. 1(c). In addition, the higher level of acoustic vibration (or acoustic power flow) in the pillars [as seen from Fig. 1(c)] causes the corresponding dispersion branches to flatten, which is another indication of the local resonance behavior.

In Figs. 1(d) and 1(e), we provide the simulated transmission of Rayleigh waves emitted and collected by a pair of IDTs (incorporated in the simulation) along the Γ - K and Γ - X directions. We choose this configuration to mimic our characterization arrangement [see Fig. 3(a)] to obtain the PnBG of the fabricated PnC. By comparing the PnBG predicted by the unit-cell band structure [i.e., Fig. 1(a)] with the transmission spectrum of the PnC structure [i.e., Figs. 1(d) and 1(e)], we realize a difference between them in the Γ - X direction. This difference is due to the presence of a deaf band at frequencies below the directional PnBG in the Γ - X direction. A deaf band is a frequency range of attenuation in the transmission of acoustic waves through a PnC beyond the actual directional PnBG; it is caused by poor coupling between the acoustic waves emitted from the IDTs and the phononic modes of the PnC adjacent to the PnBG region because of the impedance (or group-velocity) mismatch and/or polarization (or symmetry) mismatch [28,57]. Figure 2 illustrates the mode profiles of points E and F in Fig. 1, which are adjacent to the directional PnBG in the Γ - X direction. As the displacement profiles U_x and U_z for the SAW-PnC mode marked by F show, an incident Rayleigh SAW emitted from IDTs in the Γ - X direction (i.e., along the x axis in Fig. 2) can couple to mode F because of its vibration resemblance with the Rayleigh mode whose phase front lies in the y - z plane. Therefore, the simulation results do not show a deaf band for the upper frequencies of the PnBG in the Γ - X direction. However, the vibration profile of the SAW-PnC mode marked by E (see Fig. 2) indicates the formation of a deaf band for frequencies below the directional PnBG in the Γ - X direction because of the asymmetric vibration profile of the SAW-PnC mode in the x and z directions, as verified by the simulated phononic transmission shown in Fig. 1(e). In addition, the symmetries of the vibration profile of mode B in the z

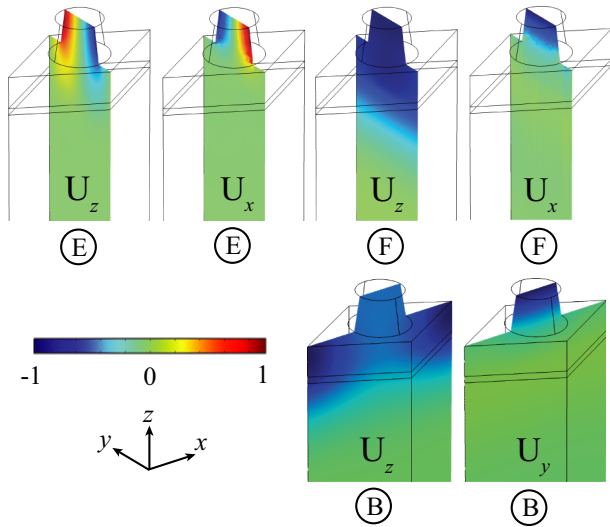


FIG. 2. Displacement profiles for modes B, E, and F, as specified in Fig. 1, on the central cut perpendicular to the flow of the acoustic power propagating along the Γ - K direction (or the y axis, mode B) and the Γ - X direction (or the x axis, modes E and F). U_x , U_y , and U_z show mode profiles of vibration along the x axis, y axis, and z axis, respectively.

and y directions depicted in Fig. 2 resemble those of the Rayleigh wave. Therefore, the deaf band at frequencies below the directional PnBG along the Γ - K direction is not noticeable.

B. Designing wideband surface IDTs

To experimentally demonstrate the predicted large PnBG of the structure, we design three wideband slanted IDTs [18,58,59], each covering 150-MHz bandwidth in the vicinity of the expected PnBG range. Figure 3(a) shows an optical micrograph of one of the fabricated devices with slanted excitation and receiver IDTs. The designed wideband slanted IDTs are formed by gradually changing the width of the metal strips and the distance between them across the aperture of the IDTs, according to the dispersion (or wavelength) of the Rayleigh-type SAW under the loading of the metal strips. We can imagine the slanted IDTs as many narrow flat-aperture single-frequency IDTs connected in parallel. The advantage of slanted IDTs over wideband unchirped apodized IDTs and wideband chirped IDTs is their maximum use of the area underneath the IDTs for transduction, which lowers their input impedance, and the launching of more acoustic power to each frequency, respectively. To avoid acoustic beam steering and yet obtain a wide fractional bandwidth, we incorporate symmetrical 500- μ m-wide-aperture slanted IDTs and limit finger slant angles to $\pm 2^\circ$. It is worth highlighting that in a multilayer substrate (i.e., a stack of multiple thin-film elastic materials on a semi-infinite substrate), the medium can be single mode or multimode, depending on the frequency of operation. As the frequency increases, higher-order surface modes begin to propagate. In our case, we limit our design to the frequency range in which our substrate allows only the fundamental Rayleigh-type SAW emitted by the slanted IDTs (see Appendix A for further discussion).

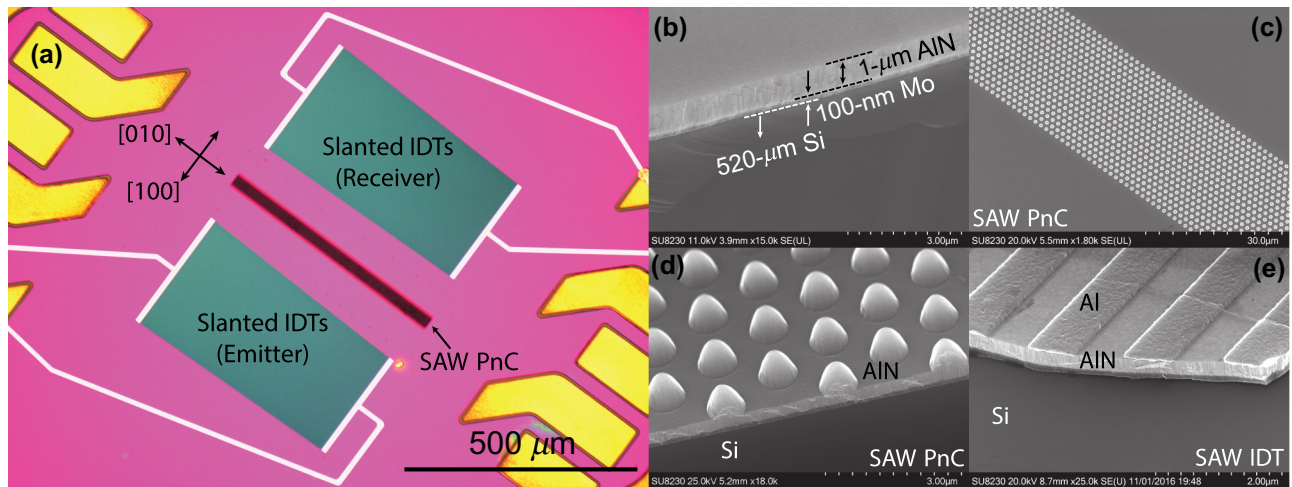


FIG. 3. Fabricated pillar-based SAW-PnC structures. (a) Optical image of the SAW-PnC device showing a ribbon of the SAW PnC between a pair of wideband slanted IDTs (emitter and receiver transducers) connected to Cu contact pads. The crossed arrows show the crystallographic orientation of silicon (100) substrate with respect to the SAW PnC. (b) SEM image of the cross section of the starting substrate for the SAW PnCs showing the material stack of 1- μ m AlN/100-nm Mo/520- μ m Si. (c) SEM image of the SAW PnC labeled in (a) for study of the SAW PnBG in the Γ - X direction. (d) Tilted SEM image of the cross section of the SAW PnC. The conelike AlN pillars are etched to 530-nm height with plasma dry etching. (e) SEM image of the cross section of the slanted IDTs showing 80-nm-thick Al metal strips fabricated on 470-nm-thick AlN after we etch 530 nm of AlN to form the pillars on the substrate.

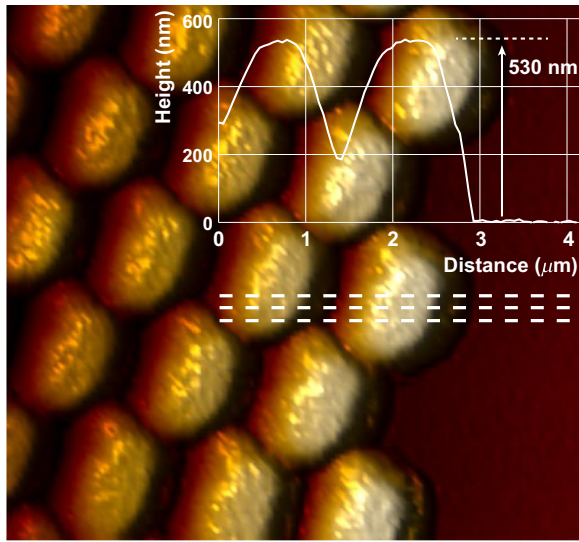


FIG. 4. AFM measurement of a fabricated pillar-based SAW PnC. The inset provides the height variation averaged over three paths highlighted by the white dashed lines, which show that the height of the fabricated pillars is 530 nm.

IV. FABRICATION AND EXPERIMENTAL RESULTS

The fabrication of our SAW-PnC structures [Fig. 3(a)] can be divided into three key steps: (1) fabricating the

AlN pillars, (2) fabricating copper (Cu) contact pads, and (3) fabricating aluminum (Al) IDTs. A cross-section scanning-electron-microscopy (SEM) image of the starting substrate, a stack of 1- μm AlN/100-nm molybdenum (Mo)/520- μm Si, for the fabrication of the SAW PnC is shown in Fig. 3(b). AlN is sputtered (by Tegal Corporation) with the c axis perpendicular to the surface of (100)-oriented highly resistive Si substrates. The high resistivity of the Si substrate minimizes the electromagnetic feedthrough coupling between the IDTs, interconnection wiring, and contact pads. Figure 3(a) shows a microscope image of one of the final fabricated SAW devices containing a SAW PnC, slanted IDTs, and contact pads. Appendix B details the fabrication of the SAW PnC. Figure 4 shows an atomic-force-microscopy (AFM) image of the final pillars, which can accurately capture the height of the pillars. However, the pillars in the AFM measurements appear slightly laterally deformed due to the finite width of the AFM tip and limited scanning resolution.

To characterize the fabricated SAW-PnC structures, we use an HP 8753D network analyzer connected to a pair of Infinity Probe probes from Cascade Microtech to measure the S_{21} parameter [i.e., transmission through the SAW-PnC structure between the emitter and receiver IDTs in Fig. 3(a)]. The data acquisition is performed with 30-kHz resolution from 1.3 to 1.85 GHz. The raw data obtained from the network analyzer are a mixture of electromagnetic and acoustic signals [60]. The

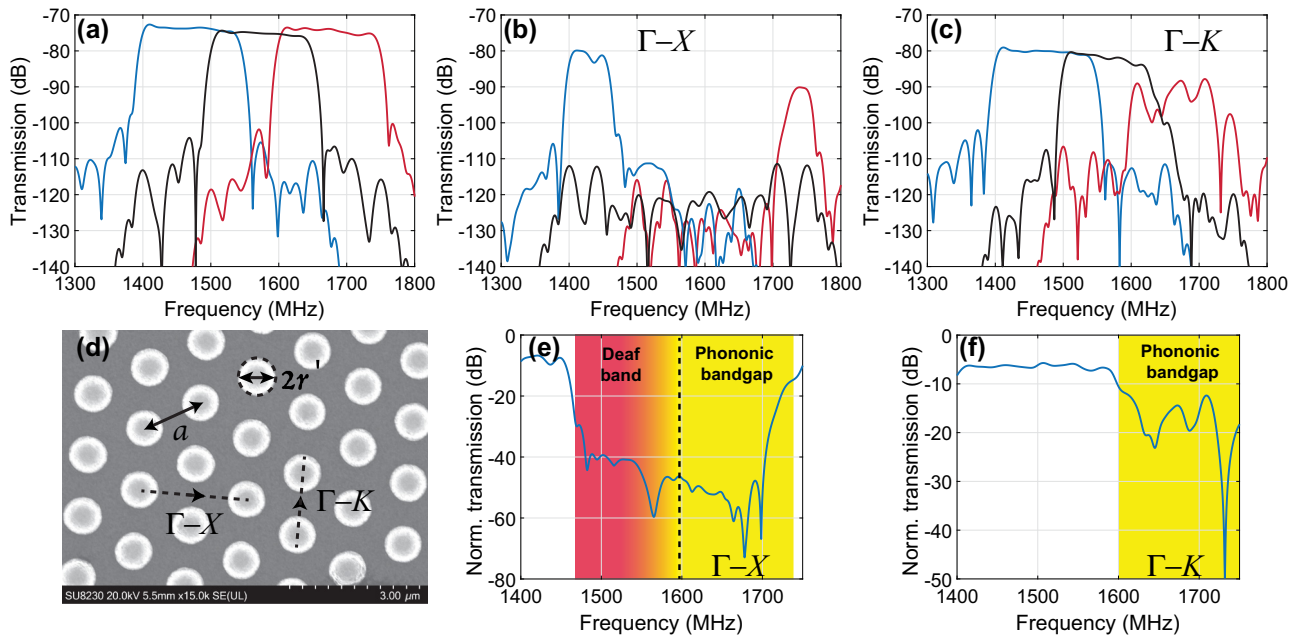


FIG. 5. S_{21} characterization of the fabricated SAW PnC. (a) The acoustic response of the three reference slanted IDTs used to measure the surface PnBG. (b),(c) Transmission of the reference IDTs with a SAW PnC in between along Γ - X and Γ - K , respectively, as defined in (d). (e),(f) Transmission of a surface acoustic wave through the surface PnC normalized to the response of the reference IDTs. The transmission drop in (e),(f) indicates the existence of a surface PnBG that considerably attenuates the passing SAW. The dashed line in (e) shows the edge of the calculated directional PnBG along Γ - X .

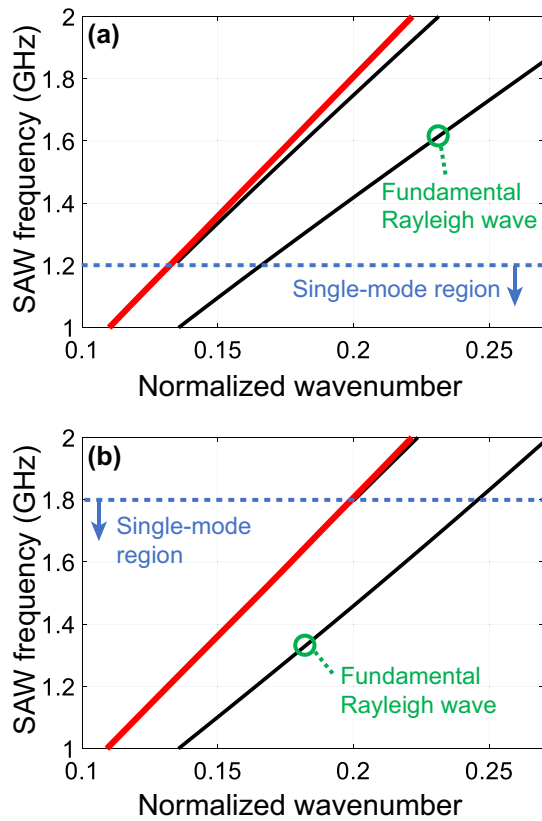


FIG. 6. Dispersion of surface acoustic waves on AlN/Mo/Si substrates. The red line indicates the sound line (or the dispersion of the slowest bulk mode in the Si substrate) and the black lines represent surface acoustic waves propagating on the surface of the AlN/Mo/Si substrate for AlN thickness of (a) $0.2 \mu\text{m}$ and (b) $0.5 \mu\text{m}$.

electromagnetic contribution comes from the capacitance that forms between input and output interconnects. The electromagnetic feedthrough can be minimized by appropriate shielding or isolation of SAW IDTs. To extract the transmitted acoustic signal from the mixed signal, we take an inverse Fourier transform and examine the signal in the time domain. Owing to the difference between the propagation speeds of the electromagnetic waves and the surface acoustic waves, the acoustic portion is well separated from the electromagnetic feedthrough in the time domain. After applying a lossless time-domain filter and taking the Fourier transform, we recover the acoustic signal in the frequency domain.

The plots in Fig. 5 provide the acoustic characterization results. In Fig. 5(a), we show the acoustic response of three wideband reference IDTs (i.e., the transmission between the input and output IDTs with no SAW PnC in between) covering 1.4–1.55 GHz (blue line), 1.5–1.65 GHz (black line), and 1.6–1.75 GHz (red line), indicating a dynamic range of more than 50 dB. Transmitted signals are measured along two major crystallographic directions: Γ - X (nine PnC periods: $9 \times a\sqrt{3}$) and Γ - K (14 PnC periods:

$14 \times a$) [see Fig. 5(d) for the definition of the directions]. The transmitted acoustic signal detected by the receiver IDTs is depicted in Figs. 5(b) and 5(c) for the Γ - X and Γ - K directions, respectively. By normalizing the transmitted acoustic signal to the response of the reference IDTs [see Fig. 5(a)], we extract the frequency profile of the attenuation for the transmitted acoustic signal [see Figs. 5(e) and 5(f)]. The frequency ranges corresponding to the directional PnBGs and the deaf band (as discussed in Sec. III A) are highlighted by the shaded yellow and red regions in Figs. 5(e) and 5(f). The experimental results reveal an at-least 150-MHz-wide PnBG at 1.65 GHz along the Γ - X direction. The results of characterization along the Γ - K direction also reveal an at-least 150-MHz-wide PnBG centered at about 1.65 GHz. Comparison of the results in Figs. 1 and 5 shows good agreement between simulations and experiments in terms of the PnBG and the presence of the deaf band.

The results in Fig. 5 clearly show the existence of hypersonic PnBGs in SAW PnCs formed without use of metallic pillars. The relatively large PnBG (10% PnBG width to center frequency) enables the formation of functional SAW devices by use of line and point defects for many applications, including wireless communication filters.

V. CONCLUSIONS

We demonstrate a platform for designing SAW-PnC devices with the PnBG in the hypersonic frequency regime. The pillars in our platform are nonmetallic, so they can reduce the overall phononic material loss and enable the formation of practical SAW-PnC devices for commercial applications requiring monolithic integration as well as scientific applications requiring low-loss SAW waveguides and high-quality SAW resonators. Because of the fewer fabrication steps for the proposed SAW PnC and the selection of the materials (i.e., AlN and Si), the platform is an ideal candidate for SAW devices integrated with CMOS circuits on a single chip for multifrequency wireless applications. This PnC platform can enable the realization of low-loss surface phononic devices, which is of great importance for next-generation phononic-based filtering circuits.

ACKNOWLEDGMENTS

This work was supported by the National Science Foundation (NSF) under Grant No. ECCS-1310340 and was performed in part at the Georgia Tech Institute for Electronics and Nanotechnology, a member of the National Nanotechnology Coordinated Infrastructure, which is supported by the NSF (Grant No. ECCS-1542174). The authors thank Reza Pourabolghasem for helpful discussions on this paper and also Hossein Taghinejad for the AFM image of the SAW PnC.

APPENDIX A: DISPERSION OF SURFACE ACOUSTIC WAVES IN PLANAR ALN/MO/SI SUBSTRATES

The plots in Fig. 6 show dispersion of SAWs for two AlN thicknesses (0.2 and 0.5 μm) on 100-nm-thick Mo on Si. Because of the multilayer nature of the selected substrate, higher-order surface modes in addition to the fundamental Rayleigh wave are allowed to propagate at high frequencies. Thus, each structure has a single-mode operation in a limited range of frequencies. It is also clear that in the thinner AlN film, the bandwidth of the single-mode operation is smaller. Having more than one mode emitted from IDTs within the frequency range of the SAW PnBG degrades the performance of the IDTs in terms of emitting desired Rayleigh-type acoustic modes. Therefore, we choose a range of frequencies over which the IDTs remain single mode.

APPENDIX B: SAW-PnC FABRICATION PROCESS

The AlN/Mo/Si substrate is first spin-coated with poly(methyl methacrylate) positive electron-beam resist and then the SAW-PnC pattern is transferred to the resist with use of a JEOL JBX-9300FS electron-beam-lithography system. We add the proximity error correction to minimize slight dimension variation throughout the phononic crystal lattice due to the back scattering of electrons during the exposure. After development of poly(methyl methacrylate), chromium (Cr) is evaporated and lifted off to create a hard etching mask for the subsequent 530-nm etching of AlN in $\text{Cl}_2/\text{BCl}_3/\text{Ar}$ etching chemistry [61]. After dry etching of AlN pillars and wet etching of the remaining Cr hard mask [see Figs. 3(c) and 3(d)], we fabricate contact pads by patterning the sputtered film of 400-nm Cu, aligned with AlN pillars, through a lift-off process using optical lithography and a positive photoresist. We then fabricate Al IDTs on the 470-nm-thick AlN by first patterning ZEP (ZEP520A by Zeon corporation) positive electron-beam resist by electron-beam lithography followed by electron-beam evaporation and lift off of 80-nm Al [Fig. 3(e)].

-
- [1] P. Hess, Surface acoustic waves in material science, *Phys. Today* **55**, 42 (2002).
 - [2] C. Campbell, *Surface Acoustic Wave Devices for Mobile and Wireless Communications* (Academic Press, New York, 1998).
 - [3] R. Aigner, in *2008 IEEE Ultrasonics Symposium* (IEEE, Beijing, China, 2008), p. 582.
 - [4] M. Metcalfe, S. M. Carr, A. Muller, G. S. Solomon, and J. Lawall, Resolved Sideband Emission of InAs/GaAs Quantum Dots Strained by Surface Acoustic Waves, *Phys. Rev. Lett.* **105**, 037401 (2010).

- [5] M. V. Gustafsson, P. V. Santos, G. Johansson, and P. Delsing, Local probing of propagating acoustic waves in a gigahertz echo chamber, *Nat. Phys.* **8**, 338 (2012).
- [6] M. V. Gustafsson, T. Aref, A. F. Kockum, M. K. Ekström, G. Johansson, and P. Delsing, Propagating phonons coupled to an artificial atom, *Science* **346**, 207 (2014).
- [7] M. J. A. Schuetz, E. M. Kessler, G. Giedke, L. M. K. Vandersypen, M. D. Lukin, and J. I. Cirac, Universal Quantum Transducers Based on Surface Acoustic Waves, *Phys. Rev. X* **5**, 031031 (2015).
- [8] Si-Yuan Yu, Xiao-Chen Sun, Xu Ni, Qing Wang, Xue-Jun Yan, Cheng He, Xiao-Ping Liu, Liang Feng, Ming-Hui Lu, and Yan-Feng Chen, Surface phononic graphene, *Nat. Mater.* **15**, 1243 (2016).
- [9] R. Manenti, M. J. Peterer, A. Nersisyan, E. B. Magnusson, A. Patterson, and P. J. Leek, Surface acoustic wave resonators in the quantum regime, *Phys. Rev. B* **93**, 041411 (2016).
- [10] Maurício M. de Lima, Jr. and Paulo V. Santos, Modulation of photonic structures by surface acoustic waves, *Rep. Prog. Phys.* **68**, 1639 (2005).
- [11] D. A. Fuhrmann, S. M. Thon, H. Kim, D. Bouwmeester, P. M. Petroff, A. Wixforth, and H. J. Krenner, Dynamic modulation of photonic crystal nanocavities using gigahertz acoustic phonons, *Nat. Photon.* **5**, 605 (2011).
- [12] Huan Li, Semere A. Tadesse, Qiyu Liu, and Mo Li, Nanophotonic cavity optomechanics with propagating acoustic waves at frequencies up to 12 GHz, *Optica* **2**, 826 (2015).
- [13] Yukihiko Tanaka and Shin-ichiro Tamura, Surface acoustic waves in two-dimensional periodic elastic structures, *Phys. Rev. B* **58**, 7958 (1998).
- [14] F. Meseguer, M. Hologado, D. Caballero, N. Benaches, J. Sánchez-Dehesa, C. López, and J. Llinares, Rayleigh-wave attenuation by a semi-infinite two-dimensional elastic-band-gap crystal, *Phys. Rev. B* **59**, 12169 (1999).
- [15] Tsung-Tsong Wu, Zi-Gui Huang, and S. Lin, Surface and bulk acoustic waves in two-dimensional phononic crystal consisting of materials with general anisotropy, *Phys. Rev. B* **69**, 094301 (2004).
- [16] V. Laude, M. Wilm, S. Benchabane, and A. Khelif, Full band gap for surface acoustic waves in a piezoelectric phononic crystal, *Phys. Rev. E* **71**, 036607 (2005).
- [17] T. Gorishnyy, C. K. Ullal, M. Maldovan, G. Fytas, and E. L. Thomas, Hypersonic Phononic Crystals, *Phys. Rev. Lett.* **94**, 115501 (2005).
- [18] Tsung-Tsong Wu, Liang-Chen Wu, and Zi-Gui Huang, Frequency band-gap measurement of two-dimensional air/silicon phononic crystals using layered slanted finger interdigital transducers, *J. Appl. Phys.* **97**, 094916 (2005).
- [19] S. Benchabane, A. Khelif, J.-Y. Rauch, L. Robert, and V. Laude, Evidence for complete surface wave band gap in a piezoelectric phononic crystal, *Phys. Rev. E* **73**, 065601 (2006).
- [20] A. Khelif, Y. Achaoui, S. Benchabane, V. Laude, and B. Aoubiza, Locally resonant surface acoustic wave band gaps in a two-dimensional phononic crystal of pillars on a surface, *Phys. Rev. B* **81**, 214303 (2010).
- [21] Y. Achaoui, A. Khelif, S. Benchabane, L. Robert, and V. Laude, Experimental observation of locally-resonant and

- bragg band gaps for surface guided waves in a phononic crystal of pillars, *Phys. Rev. B* **83**, 104201 (2011).
- [22] M. Oudich and M. B. Assouar, Surface acoustic wave band gaps in a diamond-based two-dimensional locally resonant phononic crystal for high frequency applications, *J. Appl. Phys.* **111**, 014504 (2012).
- [23] A. Khelif, Y. Achaoui, and B. Aoubiza, Surface acoustic waves in pillars-based two-dimensional phononic structures with different lattice symmetries, *J. Appl. Phys.* **112**, 033511 (2012).
- [24] B. Graczykowski, S. Mielcarek, A. Trzaskowska, J. Sarkar, P. Hakonen, and B. Mroz, Tuning of a hypersonic surface phononic band gap using a nanoscale two-dimensional lattice of pillars, *Phys. Rev. B* **86**, 085426 (2012).
- [25] D. Yudistira, A. Boes, B. Graczykowski, F. Alzina, L. Y. Yeo, C. M. Sotomayor Torres, and A. Mitchell, Nanoscale pillar hypersonic surface phononic crystals, *Phys. Rev. B* **94**, 094304 (2016).
- [26] M. Sigalas and E. N. Economou, Elastic and acoustic wave band structure, *J. Sound Vibration* **158**, 377 (1992).
- [27] M. S. Kushwaha, P. Halevi, L. Dobrzynski, and B. Djafari-Rouhani, Acoustic Band Structure of Periodic Elastic Composites, *Phys. Rev. Lett.* **71**, 2022 (1993).
- [28] J. V. Sánchez-Pérez, D. Caballero, R. Martínez-Sala, C. Rubio, J. Sánchez-Dehesa, F. Meseguer, J. Llinares, and F. Gálvez, Sound Attenuation by a Two-Dimensional Array of Rigid Cylinders, *Phys. Rev. Lett.* **80**, 5325 (1998).
- [29] A. Khelif and A. Adibi, *Phononic Crystals: Fundamentals and Applications* (Springer, New York, 2016).
- [30] John D. Joannopoulos, Steven G. Johnson, Joshua N. Winn, and Robert D. Meade, *Photonic Crystals: Molding the Flow of Light* (Princeton University Press, Princeton, NJ, 2008).
- [31] R. Dehghannasiri, R. Pourabolghasem, A. A. Eftekhar, and A. Adibi, Integrated phononic crystal resonators based on adiabatically-terminated phononic crystal waveguides, *AIP Adv.* **6**, 121603 (2016).
- [32] R. Pourabolghasem, R. Dehghannasiri, A. A. Eftekhar, and A. Adibi, Waveguiding Effect in the Gigahertz Frequency Range in Pillar-based Phononic-Crystal Slabs, *Phys. Rev. Appl.* **9**, 014013 (2018).
- [33] Tsung-Tsong Wu, Zi-Gui Huang, Tzu-Chin Tsai, and Tzung-Chen Wu, Evidence of complete band gap and resonances in a plate with periodic stubbed surface, *Appl. Phys. Lett.* **93**, 111902 (2008).
- [34] Y. Pennec, B. Djafari Rouhani, H. Larabi, A. Akjouj, J. N. Gillet, J. O. Vasseur, and G. Thabet, Phonon transport and waveguiding in a phononic crystal made up of cylindrical dots on a thin homogeneous plate, *Phys. Rev. B* **80**, 144302 (2009).
- [35] Mourad Oudich, Yong Li, Badreddine M. Assouar, and Zhilin Hou, A sonic band gap based on the locally resonant phononic plates with stubs, *New J. Phys.* **12**, 083049 (2010).
- [36] R. Pourabolghasem, A. Khelif, S. Mohammadi, A. A. Eftekhar, and A. Adibi, Physics of band-gap formation and its evolution in the pillar-based phononic crystal structures, *J. Appl. Phys.* **116**, 013514 (2014).
- [37] B. A. Auld, *Acoustic Fields and Waves in Solids* (John Wiley, New York, 1973).
- [38] J. Segovia-Fernandez and G. Piazza, Thermoelastic damping in the electrodes determines Q of AlN contour mode resonators, *J. Microelectromech. Syst.* **26**, 550 (2017).
- [39] A. N. Cleland, *Foundations of Nanomechanics* (Springer-Verlag, Berlin, 2013).
- [40] Shirin Ghaffari and Thomas William Kenny, *Resonant MEMS: Fundamentals, Implementation, and Application* (Wiley, Weinheim, Germany, 2015), p. 55.
- [41] C. Zener, Internal friction in solids II. General theory of thermoelastic internal friction, *Phys. Rev.* **53**, 90 (1938).
- [42] C. Zener, *Elasticity and Anelasticity of Metals* (University of Chicago Press, Chicago, Illinois, 1948).
- [43] A. S. Nowick and B. S. Berry, *Anelastic Relaxation in Crystalline Solids* (Academic Press, New York, 1972), Vol. 1.
- [44] L. D. Landau and E. M. Lifshitz, *Theory of Elasticity* (Pergamon Press, Oxford, 1995), 3rd ed.
- [45] Ron Lifshitz and M. L. Roukes, Thermoelastic damping in micro- and nanomechanical systems, *Phys. Rev. B* **61**, 5600 (2000).
- [46] Sudipto K. De and N. R. Aluru, Theory of thermoelastic damping in electrostatically actuated microstructures, *Phys. Rev. B* **74**, 144305 (2006).
- [47] S. Vengallatore, Analysis of thermoelastic damping in laminated composite micromechanical beam resonators, *J. Micromech. Microeng.* **15**, 2398 (2005).
- [48] M. Ashby, *Materials Selection in Mechanical Design* (Butterworth-Heinemann, Oxford, 2011), 4th ed.
- [49] W. P. Mason and H. E. Bommel, Ultrasonic attenuation at low temperatures for metals in the normal and superconducting states, *J. Acoust. Soc. Am.* **28**, 930 (1956).
- [50] A. Frangi, M. Cremonesi, A. Jaakkola, and T. Pensala, Analysis of anchor and interface losses in piezoelectric mems resonators, *Sensors Actuators A: Phys.* **190**, 127 (2013).
- [51] Li-Wen Hung and Clark T. C. Nguyen, Capacitive-piezoelectric transducers for high-Q micromechanical AlN resonators, *J. Microelectromech. Syst.* **24**, 458 (2015).
- [52] R. M. White and F. W. Voltmer, Direct piezoelectric coupling to surface elastic waves, *Appl. Phys. Lett.* **7**, 314 (1965).
- [53] Gianluca Piazza, Valeriy Felmetzger, Paul Mural, Roy H. Olsson, III, and Richard Ruby, Piezoelectric aluminum nitride thin films for microelectromechanical systems, *MRS Bull.* **37**, 1051 (2012).
- [54] Joerg Bochmann, Amit Vainsencher, David D. Awschalom, and Andrew N. Cleland, Nanomechanical coupling between microwave and optical photons, *Nat. Phys.* **9**, 712 (2013).
- [55] Krishna C. Balram, Marcelo I. Davanco, Jin Dong Song, and Kartik Srinivasan, Coherent coupling between radiofrequency, optical and acoustic waves in piezo-optomechanical circuits, *Nat. Photon.* **10**, 346 (2016).
- [56] <https://www.comsol.com>.
- [57] R. Pourabolghasem, S. Mohammadi, A. A. Eftekhar, A. Khelif, and A. Adibi, Experimental evidence of high-frequency complete elastic bandgap in pillar-based phononic slabs, *Appl. Phys. Lett.* **105**, 231908 (2014).

- [58] C. K. Campbell, Yanglin Ye, and J. J. Sferrazza Papa, Wide-band linear phase saw filter design using slanted transducer fingers, *IEEE Tran. Sonics Ultrason.* **29**, 224 (1982).
- [59] H. Yatsuda, Design techniques for saw filters using slanted finger interdigital transducers, *IEEE Tran. Ultrason. Ferroelectr. Frequency Control* **44**, 453 (1997).
- [60] J. H. Visser and A. Venema, in *IEEE 1988 Ultrasonics Symposium Proceedings* (IEEE, Beijing, 1988), Vol. 1, p. 297.
- [61] Chi Xiong, Wolfram H. P. Pernice, and Hong X. Tang, Low-loss, silicon integrated, aluminum nitride photonic circuits and their use for electro-optic signal processing, *Nano Lett.* **12**, 3562 (2012).